Hybrid Rocket Engines Optimized by Multi-Stepped Design Approach: Experimental Investigation

Christopher Glaser, Jouke Hijlkema, Jean-Yves Lestrade, Jérôme Anthoine

Hybrid Rocket Engines Optimized by Multi-Stepped Design Approach: Experimental Investigation

By Christopher GLASER,[1),*] Jouke HIJLKEMA,[1)], Jean-Yves LESTRADE,[1)] and Jérôme ANTHOINE[1)]

[1)] *ONERA/DMPE, Université de Toulouse, F-31410 Mauzac*
** christopher.glaser@onera.fr*

We investigate a new design approach to increase the performance and versatility of Hybrid Rocket Engines. The concept is to calculate optimized fuel grain profiles according to different criteria (lower oxidizer-to-fuel ratio (O/F) shift and O/F values closer to stoichiometry) using a genetic algorithm. These idealized profiles are then approximated by a set of steps. Due to the steps, the turbulence and, thus, the regression rate of the engine increases. We show that the regression rate can be increased by up to 80 % if only the regression rate needs to be increased to a maximum. With the optimized profiles, we increase the regression rate by up to 58 % while also achieving O/F values closer to stoichiometry. A lower oxidizer-to-fuel shift could not be conclusively proven. The genetic algorithm initially developed to optimize hybrid fuel profiles was adapted to also allow deriving spatially resolved Marxman laws using only one test firing. We prove that the regression rate increase through steps can be accumulated with multiple steps. This way, we laid the foundation to create even more complex fuel grain geometries by a set of fuel grain slices. For optimization with the genetic algorithm, however, the full potential needs to be assessed on larger motors and longer burn times. This is because our hybrid engine in the investigated firing times burns already rather uniform, giving us fewer possibilities to optimize the profiles. Nevertheless, the genetic algorithm turned out to be a powerful tool to obtain empirical Marxman values for regression rate prediction, while for optimization of profiles other means than the genetic algorithm should be investigated in parallel.

Key Words: Hybrid Rocket, Stepped Design, Regression Rate, Optimized Design

Nomenclature

a	:	marxman constant	n_p	:	number of fuel ports
A_t	:	nozzle throat area	P	:	population
$A_{i,j}$	:	port area at index i, j	P_c	:	chamber pressure
b	:	marxman constant	Q_i	:	quality criterion
$c*$	:	characteristic velocity	$\mathscr{R}$	:	crossbreeding operator
C_i	:	polynomial coefficient	$\dot{r}$	:	regression rate
$D_{i,j}$	:	port diameter at index i, j	$S_{i,j}$	:	burning surface at index i, j
D_f	:	final port diameter	t_b	:	burn time
D_0	:	initial port diameter	$V_{\text{init/end}}$	:	initial and end volume
D_{exp}	:	final experimental diameter	w_i	:	weight of quality criterion
G	:	mass flux	x	:	axial coordinate
G_{ox}	:	oxidizer mass flux	x/h	:	step to height ratio
I	:	individual	ρ	:	fuel density
L	:	fuel port length	η	:	c* combustion efficiency
L_g	:	fuel grain length	ϵ	:	random number
Δm_f	:	mass loss			
$\dot{m}_{\text{ox}}$	:	oxidizer mass flow			
$\dot{m}_{\text{fuel}}$	:	fuel mass flow			
$\dot{m}_{i,j}$	:	total mass flow at index i, j			
$\mathscr{M}$	:	mutation operator			
n	:	marxman constant			

1. Introduction

The versatility of Hybrid Rocket Engines (HREs) in terms of propellant choice, throttleability and overall application is well known. However, challenges like low regression rates, high fuel residuals, Oxidizer-to-fuel (O/F) shift and the overall inferior maturity of HREs are limiting the widespread utilization of HREs in the space domain. In previous work,[1,2] we proposed a novel approach to tackle low regression rates, O/F shift and residuals in one design. Additionally, this proposed stepped design approach can potentially increase the overall versatility of HREs because it allows tailoring the engines' performance exactly to the envisioned use-case. The concept is to use multiple fuel grain segments rather than one single grain. The different fuel grain segments or slices can have different inner diameters (or any other desired geometric characteristic) and assembled together they represent a fuel grain geometry that is approximated by steps. Due to the steps, mixing and turbulence increase due to the formation of recirculation zones. As a consequence, the regression rate increases too. This enables advanced geometries (even helical designs[3]) that otherwise would need to be printed, which can limit fuel choice, density control and large scale applications. In the present work, we calculate optimized fuel grain profiles according to different criteria (such as low O/F shift or residuals) using a genetic algorithm. The genetic algorithm allows also to estimate the spatially resolved Marxman fit in the form of:[4]

$$\dot{r} = a \cdot G^n \cdot x^b \,, \tag{1}$$

where $\dot{r}$ is the time-averaged regression rate, G the total mass flux, x the axial coordinate and a, b, n empirical parameters that best fit the experiments. Usually, to obtain the empirical parameters, multiple experiments need to be performed. With the genetic algorithm, a single test firing can suffice.

Our previous work concentrated on the numerical and experimental investigation of a single step (both backward- and forward facing) inside the engine. Numerically[1] and experimentally[2] the regression rate increased locally due to the increased mixing of the single step. Moreover, an important length-to-height relationship of the zone of influence of steps was derived. Using these experimental data allows to approximate full profiles by multiple steps for this paper. This work therefore is a direct continuation of previous efforts.

The article is structured as follows: first, literature relevant to our case is explained. Then, the genetic algorithm to generate semi-optimized profiles is explained. Finally, three profiles are approximated by steps and the experimental results discussed.

2. Stepped Designs in the Literature

Numerous designs to increase the regression rate can be found in the HRE literature,[5,6] however, the literature on steps in hybrids is limited. Korting *et al.*[7] tested a BFS at the entrance of their hybrid motor. Locally, the regression rate doubled compared to the reference cases due to the formation of a recirculation zone. In fact, the highest regression rate could be traced back to the point of the re-attachment of the flow after the recirculation zone. Moreover, Korting *et al.*[7] tested different oxidizer mixtures (ranging from 100 % pure oxygen to 20 % oxygen with 80 % nitrogen). Interestingly, for mixtures with only 20 % oxygen, combustion only occurred when the stepped design was used. In a reference case without step at 20 % oxygen, the motor would not ignite. The explanation for this phenomenon lies in the increased mixing due to the recirculation zone after the step. For low oxygen environments, the base-line mixing of the reference cases was not enough to promote ignition.

Kamps *et al.*[8] included a BFS in the middle of their motor (10 mm height) to augment mixing. Directly after the step, the regression rate decreased shortly (inside the recirculation zone length) to then display a local maximum in regression rate. Lee *et al.*[9] investigated the use of a BFS (5–7.5 mm height), to not only increase the regression rate, but also to decrease the pressure oscillations compared to a diaphragm case. The stepped design increased the average regression rate downstream the step by up to 50 % and decreased the pressure oscillations down to 4 % of the mean chamber pressure. Musa *et al.*[10] researched numerically the use of BFS and FFS in a Solid Fuel Ramjet (SFRJ) that uses High-Density Polyethylene (HDPE). Apart from the oxidizer (which is air), SFRJs have the same cylindrical combustion chambers as HREs. For this reason, they can be compared to the hybrid engine combustion. Musa *et al.*[10] stated that in the case of BFS, the regression rate directly after the step decreases drastically inside the recirculation zone to then increase considerably after the re-attachment. For FFS, the decrease in regression rate is already visible before the step, as the flame is pushed away from the fuel surface. After the step, the regression rate is higher than before (because of the difference in mass flux), with a distinct local peak in regression rate which is attained further upstream than for a BFS case.

We were able to show the effect of steps experimentally[2] and numerically[1] in previous research of a single BFS and FFS (7.5 mm each). For proper comparison, we added for each mass flux different reference cases to quantify the effect. Directly after the BFS, the local regression rate decreases under the reference because of the flame being further away from the fuel surface and the recirculation zone hindering the boundary layer to be fully developed. After the re-attachment, the regression rate increased by a constant value over the reference cases, leading to a total increase of the space and time averaged regression rates of 21 % for the BFS case for total fuel grain lengths of 500 mm and 17 % on a motor with 110 mm length. For the FFS cases, the regression rate decreases already before the step and shows a local maxima directly after the step, which is reached further upstream than for the BFS cases. Quantitatively speaking, for a total grain length of 500 mm, the space and time averaged regression rate did not increase, because the local maximum is too thin to be noticeable on a long grain. On the motor with the short grain, however, the average regression rate increased by 47 %. The reason for this behavior was found in the total fuel grain length.[2] The BFS cases have a constant increase of regression rate after the step, whereas the FFS case are more pronounced but limited in their area of influence. As a first postulation, when it comes to distributing multiple steps along a profile, FFS should be placed close to each other to prolong their area of influence whereas BFS should be given space in between them to profit from the constantly increased regression

rates.

The distribution of multiple steps has been also researched by Sakashi *et al.*[11] with a set of BFS and FFS (called concave-convex design) and heights between 3 to 9 mm. The average regression rates increased by up to 100 %. Concerning the regression rate, the step heights were more important than the step width. Interestingly, for increasing step height, the c* efficiency declined. From 96 % with a step height of 3 mm to 92 % with 6 mm step height and 91 % for 9 mm step height. The positive effects of the steps were visible both with and without swirling injection, hinting at the possibility to combine both approaches to increase the regression rate. Kumar and Joshi[12] investigated a grain with sequence of four alternating BFS/FFS. The average regression rate increased up to 55 %, well in line with the aforementioned literature.

3. Experimental Methods

This section gives a short overview of the experimental equipment and methods used to obtain experimental results.

3.1. HYCAT Test Facilities

The HRE used in this study is the HYCAT (*Hybrid with CATalyzer*[13]) engine of ONERA. It uses hydrogen peroxide (H_2O_2) in an 87.5 % concentration as oxidizer and HDPE as fuel. The hydrogen peroxide is decomposed over a catalyst and the hot decomposition products ignite the engine before the combustion gases are expanded through an ablatively cooled graphite nozzle. The temperature upstream the injector is measured. A Coriolis mass-flow meter measures the oxidizer mass flow rate, and the chamber pressure is obtained in the pre- and post-chamber by four piezo-electric pressure probes. In all our test cases, a simple axial injector is used. The total length of the fuel grain is 500 mm. The thrust is measured in x, y and z direction. Tests conducted on the HYCAT engine are abbreviated with the letter *H* followed by the number of the test, e.g., H48.

3.2. Mass Loss Method

Probably the most common method to estimate the time- and space average regression rate is the mass loss method. The fuel grain is weighed before and after the test. With the known mass loss and assuming uniform and cylindrical consumption, the final diameter of the fuel grain can be estimated as:[14]

$$D_f^2 = \frac{4\Delta m_f}{\pi \rho_f L_g} + D_0^2 \,. \tag{2}$$

Knowing the final diameter (D_f) and the initial diameter (D_0), the regression rate (averaged in space and time) can be calculated using the burn time (t_b):

$$\dot{r} = \frac{D_f - D_0}{2t_b} \,. \tag{3}$$

3.3. Longitudinal Slicing

Another method to obtain also the local regression rate profiles was presented in Ref. 2). The principle is to cut the fuel grains after the tests along their longitudinal axis. With a standard office scanner and an image processing software such as *Fiji*,[15] the local final diameter $D_f(x)$ can be obtained. The time averaged local regression rate (assuming axisymmetry) denotes therefore to:

$$\dot{r}(x) = \frac{D_f(x) - D_0(x)}{2t_b} \,. \tag{4}$$

3.4. Ballistic reconstruction

The ballistic reconstruction method deployed in our research is based on the work presented by Messineo *et al.*[16] and adopted by Quero Granado *et al.*[17] At the base, the space averaged regression rate over time is calculated with the mass balance inside the motor: the sum of injected oxidizer mass flow ($\dot{m}_{\mathrm{ox}}$) and the burnt solid propellant ($\dot{m}_{\mathrm{fuel}}$) is equal to the total mass flow through the nozzle. The mass flow through the nozzle can be estimated with the characteristic velocity c^*, nozzle throat area A_t and chamber pressure P_c. Summarizing, the mass balance denotes to:

$$\dot{m}_{\mathrm{ox}} + \dot{m}_{\mathrm{fuel}} = \frac{P_c\, A_t}{c^*} \,. \tag{5}$$

The exhaust velocity can be obtained assuming a constant combustion efficiency ($\eta = c^*/c^*_{\mathrm{theo}}$). Rearranging leads to:

$$c^*_{\mathrm{theo}} \left(1 + \frac{1}{O/F}\right) = \frac{P_c\, A_t}{\eta\, \dot{m}_{\mathrm{ox}}} \,. \tag{6}$$

With a given η (set), A_t (known) and $\dot{m}_{\mathrm{ox}}$ (measured) the O/F (and, thus, the fuel mass flow and consequently the regression rate) can be calculated at any time step. The c^*_{theo} can be calculated with tools for thermochemical equilibrium, such as CEA.[18] While the ballistic reconstruction is a powerful tool to obtain the space averaged regression rates over time, the following assumptions that can limit the prediction of the calculated regression rate are to be noted:

1. The combustion efficiency η is considered constant throughout the burn. Especially during start up and shut down phases, this assumption is not true.[16]
2. The nozzle throat diameter is set as constant, not taking into account erosion during the burn.
3. The nozzle discharge coefficient (that takes into account the non-uniformity of the flow) to correct the efficient throat diameter is not considered in this study.
4. To calculate the regression rate from the fuel mass flow, the (initial) fuel port diameter needs to be known. For uniform, cylindrical grains, the diameter is constant over the longitudinal axis. For (multi-) stepped fuel grains, this is not true. As a best approximation, the average initial fuel grain diameter is considered.
5. Due to the steps, the effective fuel surface increases for stepped grains. At the present state, our reconstruction model cannot take this effect into account.
6. The left-hand side of Eq. 6 is not monotonous, but can have three roots,[16] which makes solving the equation difficult. Messineo *et al.*[16] proposed to approximate the non-monotonous area with a linear fit.

Nonetheless, the ballistic reconstruction method allows for qualitative analyses for the development of the regression rate over time and the O/F.

4. The Genetic Algorithm

The principle of the genetic algorithm[19] can be described in a single sentence: create a population P_0 with M random individuals $I_{0,m}$, select the best individuals and crossbreed and mutate them and repeat from the beginning. The process is visualized in Fig.1. The algorithm is an adapted and improved version of the genetic algorithm presented in Ref. 19). The genetic algorithm can be used to a) optimize a fuel port profile and b) to obtain the empiric Marxman parameters a, b, n (Eq. 1) with a single test. In the respective subsections, we elaborate on the process.

4.1. Algorithm to Obtain Optimized Profiles

In the case of a genetic algorithm to (semi-) optimize fuel grain profiles, an individual I is described by a polynomial function of degree n and its polynomial coefficients C_i to describe the fuel port.[19] Theoretically, more parameters such as fuel port length L, or number of ports n_p (or any other characteristic for that matter) can be added, however, for this study, apart from the polynomial coefficients, the other parameters are fixed to $L = 500\,\text{mm}$ and $n_p = 1$. Thus, the population (a set of individuals I) is defined by:

$$P = [I_i] \mid I_i = [C_1^i, C_2^i ..., C_n^i]. \tag{7}$$

To initialize the population P_0, a number of random individuals I_0 are generated. Next, for each individual of the population, the profile is regressed to judge its performance at the end of the simulated burn. The simulation is a simplified iterative simulation, where the time (dt, index i) and 1-D space (dx, index j) are discretized:[19]

$$S_{i,j} = n_p \pi D_{i,j} dx \tag{8}$$

for the burning surface $S_{i,j}$. The fuel port Area $A_{\text{i,j}}$ can be described as:

$$A_{i,j} = 0.25 n_p \pi D_{i,j}^2 \,. \tag{9}$$

The total mass flow (oxidizer and fuel) denotes to:

$$\dot{m}_{i,j} = \dot{m}_{ox} + \sum_{k=1}^{j-1} \rho_f \dot{r}_{i,j} S_{i,j} \,. \tag{10}$$

The local regression rate is calculated using the known Marxman approach taking into account also the axial distance $x = j * dx$:

$$\dot{r}_{i,j} = \begin{cases} a \cdot \left(\frac{\dot{m}_{i,j}}{A_{i,j}}\right)^n \cdot x^b & \text{if } D_{i,j} < D_m \\ 0 & \text{if } D_{i,j} \geq D_m \,, \end{cases} \tag{11}$$

which means that the algorithm stops regressing at point j at time i once the diameter of the motor D_m is reached. The new fuel port diameter D at station j and time i is updated as:

$$D_{i+1,j} = D_{i,j} + 2\, \dot{r}_{i,j}\, dt \,. \tag{12}$$

Finally, the O/F ratio at each point j is determined as:

$$OF_i = \frac{\dot{m}_{\text{ox}}}{\dot{m}_{\text{fuel}}} = \frac{\dot{m}_{ox}}{\sum_j^N \rho_f \dot{r}_{i,j} S_{i,j}} \,. \tag{13}$$

After the total burn time (given as the total number of time steps T) is reached, the quality of each individual can be assessed based on the three criteria:

$$\text{minimal variation: } Q_1 = \frac{\max_i(OF_i) - \min_i(OF_i)}{\overline{OF_i}}$$

$$\text{optimal O/F: } Q_2 = \frac{OF_{st} - \overline{OF_i}}{\overline{OF_i}}$$

$$\text{minimal residuals: } Q_3 = \frac{V_{\text{init}} - V_{end}}{V_{\text{init}}}$$

with $V_{\text{init/end}}$ being the initial and end volume of the grain, respectively. These criteria allow sorting our individuals using a weighted approach:

$$Q_{\text{total}} = w_1 Q_1 + w_2 Q_2 + w_3 Q_3 \,. \tag{14}$$

At this point, the reproductive step of the genetic algorithm to construct a new generation of the population P_{i+1} is started:

1. Keep the best individuals n_{best}:

$$I_{n+1,m} = I_{n,m} \; \forall m \in [1, n_{best}] \,.$$

2. Crossbreed the first $2 \times n_{\text{best}}$:

$$I_{n+1,m+n_{best}} = \text{cross}(I_{2m-1}, I_{2m}) \; \forall m \in [1, n_{best}] \,.$$

3. Mutate the first n_{best} individuals:

$$I_{n+1,m+2n_{best}} = \text{mutate}(I_m) \; \forall m \in [1, n_{best}] \,.$$

4. Add the remaining $M - 3 \times n_{best}$ random individuals.

We can define the random crossbreeding $\mathscr{R}$ and mutation $\mathscr{M}$ operator with:

$$\mathscr{R}(x, y) = \begin{cases} x & : p \leq 0.5 \\ y & : p > 0.5 \end{cases}$$

$$\mathscr{M}(x, \epsilon) = x \times (1 + (1 - 2p)\epsilon) \,,$$

where $p \in [0, 1]$ is a random number and ϵ a small number (we use $\epsilon = 0.1$). This leads to:

$$\text{cross}(I, J) = [\mathscr{R}(C_1^I, C_1^J), \ldots, \mathscr{R}(C_n^I, C_n^J)]$$

$$\text{mutate}(I) = [\mathscr{M}(C_1, \epsilon), \ldots, \mathscr{M}(C_n, \epsilon)]$$

The newly generated population P_{i+1} can now be regressed again following the Equations 8-13, therefore closing the loop. The process is displayed in Figure 1. It is considered finished when either a predefined minimum quality is reached or the maximum number of iterations is reached. Given the number of dependent parameters, there is no unique optimal solution.[19] For this reason, convergence is hard to achieve. Based on previous experiences documented in Ref.19), the algorithm increases the quality of the population very fast for the first 1 000 iterations. However, for additional iterations (even up to one million iterations), the quality does not increase significantly anymore. This is why we chose 10 000 as a maximum number of iterations to save computational effort.

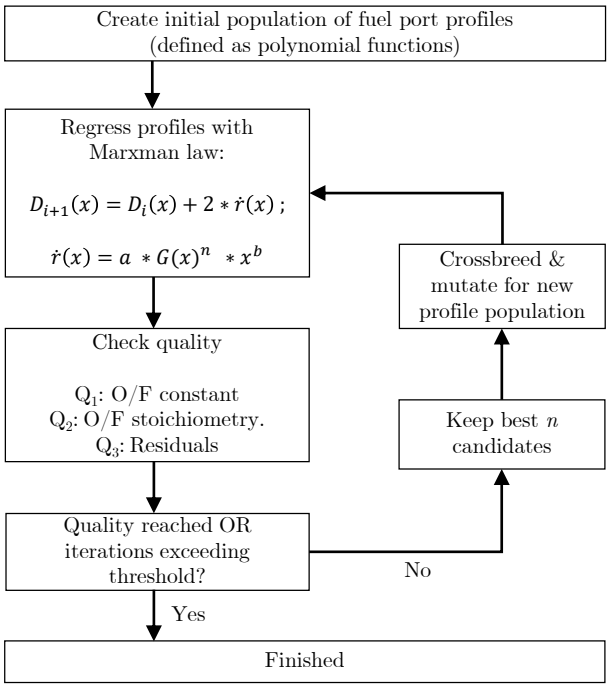

Fig. 1. The flow of the genetic algorithm in profile optimization mode.

4.2. Algorithm to Obtain Empirical Marxman Parameters

The algorithm – initially developed to calculate (semi-) optimized fuel port profiles – can also be used to obtain the spatially resolved Marxman law, which is written in Equation 1 with a single test firing. Usually, multiple tests at different diameters and mass fluxes need to be conducted to get an estimate on the Marxman law, and even then it is often not possible to estimate the axial component (x^b). With our adapted genetic algorithm, a single test suffices.

The basic principle of the genetic algorithm remains the same, but the population in this adaption are the empirical Marxman parameters a, b, n:

$$I = [a, b, n]. \tag{15}$$

The progression of the profiles are identical to Eqs. 8-13, however, the initial profile starts always at D_0 that corresponds to the test firing.

After T time steps, which correspond to the experimental duration, the numerically obtained final diameters are compared to the final fuel port diameter obtained after the experiments D_{exp} (for the process to obtain the experimental diameters, see Section **3.3.**). The quality criterion is thus defined at any station j as:

$$Q_{i=T,j} = \left| \frac{D_{\text{exp},i=T,j} - D_{i=T,j}}{D_{\text{exp},i=T,j}} \right| \tag{16}$$

and the average error denotes to:

$$\overline{Q} = \frac{\sum_0^N Q_j}{N} \, . \tag{17}$$

The population can now be sorted according to its quality and the best individuals be crossbred and mutated similar to Section **4.1.**. However, the crossbreeding and mutation operators need to be adjusted accordingly:

$$\text{cross}(I, J) = [\mathscr{R}(a^I, a^J), \mathscr{R}(b^I, b^J), \mathscr{R}(n^I, n^J)]$$
$$\text{mutate}(I) = [\mathscr{M}(a, \epsilon), \mathscr{M}(b, \epsilon), \mathscr{M}(n, \epsilon)]$$

The process is depicted in Figure 2. With this approach, it is possible to obtain the locally resolved Marxman parameters (or at least a close estimation) using only a single test.

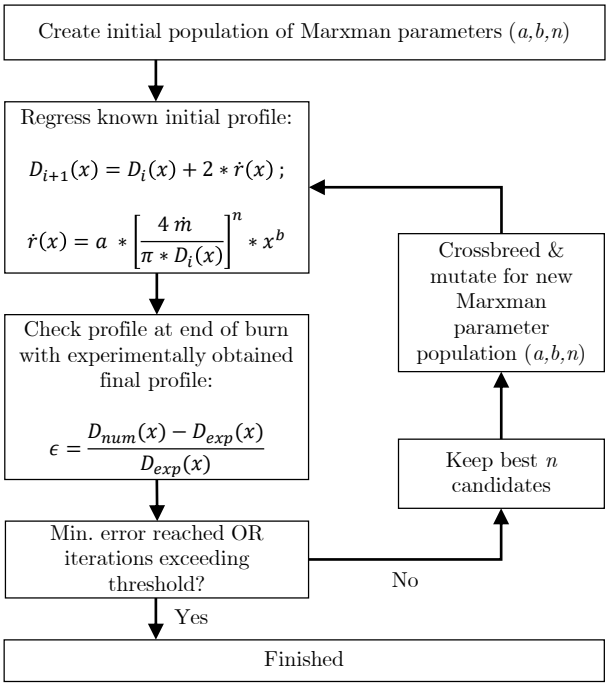

Fig. 2. The flow of the genetic algorithm in Marxman parameter mode.

4.2.1. Validation of the Algorithm in Marxman Mode

In order to validate the approach to obtain the Marxman empirical parameters, we are testing it on two reference tests (H48 and H49) that we conducted in the past. Using the longitudinal cutting method presented in Section **3.3.**, the final diameter along the fuel grain axis is obtained. Moreover, the tests were conducted at different initial fuel port diameters (25 mm and 40 mm), which allows us to assess whether the Marxman empirical constants are valid for a larger range of fuel port diameters.

Feeding the algorithm both final experimental profiles to search for the best fitting a, b, n values of the Marxman law, the results after 30 000 iterations yield the following values (for regression rate in m/s, G in kg/m^{2}s and x in m):

$$\dot{r} = 9.03 * 10^{-7} \cdot G^{1.091} \cdot x^{-0.154} \tag{18}$$

When these a, b, n values are applied to the simulations of H48 and H49, the average relative discrepancy between the final diameter of the experiment and the algorithm are 1.8 % in the case of H48 and 1.7 % with H49. These results are displayed in Figure 3 and show a satisfactory fit over the total fuel grain length, with larger discrepancies near the injector head.

5. Preparation of the Profiles

In this section, we obtain and prepare the optimized fuel port profiles for the experimental test campaign. First, we derive the Marxman law for a stepped case, then we develop the optimal profile and approximate it in two different ways with multiple steps.

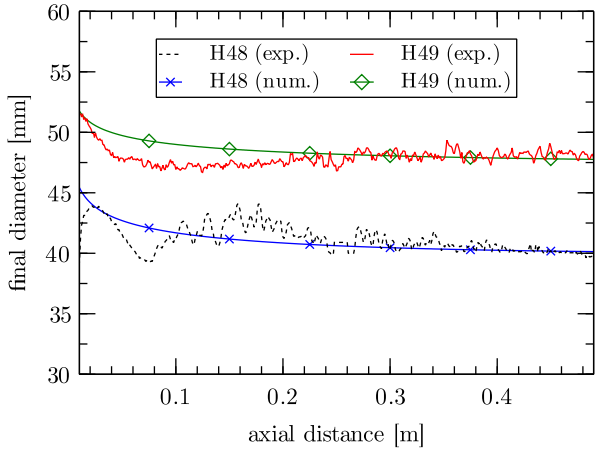

Fig. 3. Comparison of experimental final diameters and final diameters obtained with the Marxman empirical parameters.

5.1. Definition of an Alternating Stepped Reference Case

The first task is to create a reference case for a multi-stepped profile. So far, we only considered classical cylindrical fuel grains or grains with a single step.[1,2] While this was important to understand the fundamental mechanisms of steps in hybrid rocket engines, the a, b, n values of classic cylindrical grains or single stepped fuels cannot be applied to multi-stepped profiles. Thus, based on conclusions from Ref. 2), we prepared a multi-stepped profile with alternating steps to a) obtain a, b, n values for a multi-stepped grain and b) to create a multi-stepped reference in order to evaluate if an optimized profile looses some of the maximal regression rate enhancement due to the steps following a profile.

The alternating step grain is designed as a sequence of FFS and BFS with a step height of 7.5 mm. Based on Refs. 1, 2), the approach is as follows: the area of the injector effects (increased heat transfer due to recirculation zone[20]) in our HYCAT engine is noticeable up to 50 mm axial distance. This area increases the regression rate, and therefore we keep the first 50 mm of the grain unaltered. After the first 50 mm, a total of 7 alternating steps (4 BFS and 3 FFS) are employed. Following the rule of thumb developed in previous research,[1,2] the length after an BFS should be longer than for an FFS, because a BFS increases the regression rate after the step by a constant value over the reference, whereas FFS have a more pronounced but shorter area of influence. For this reason, a first alternating profile with a step-to-height ratio (x/h) of 10 for BFS and roughly 7 for FFS is decided upon. For a step height of 7.5 mm (to stay true to previous work on single steps) this translates to 75 mm length after the BFS and 50 mm after the FFS. The initial profile is illustrated in Figure 4. Generally speaking, the alternating profile consists of grain slices with either 25 mm or 40 mm inner diameter (black curve). Our cylindrical reference tests were conducted on constant 25 mm or 40 mm fuel ports. This allows us to compare the alternating stepped profile directly to the reference cases.

5.2. Derivation of Marxman Law for Multi-stepped Grains

Having defined the alternating profile, we derive the a, b, n Marxman parameters for a stepped profile in this section, because the a, b, n values calculated in Section **4.2.1.** for a cylindrical grain are not valid anymore. Therefore, the alternating step grain (labeled H55) is fired on the HYCAT engine and the weight loss of each grain slice after the test is investigated to estimate the final diameter using the mass loss method of Eq. 2. Because the multi-step grain is composed of connected fuel grain cylinders with different inner diameters, each segment can be weighed separately. Since the sole goal is to obtain the a, b, n parameters, at this stage the mass-loss method suffices in terms of accuracy. The detailed investigation of the regression rate profile (with the slicing method) of the alternating grain is carried out in Section **6.1.**. In Figure 4, the initial vs. the final diameter of the test as well as the final diameter calculated with the Marxman parameters that the algorithm calculated is shown. The resulting parameters are:

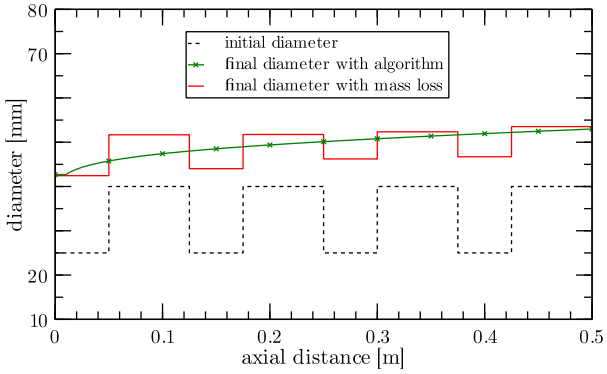

Fig. 4. Diameter profiles of H55.

$$\dot{r} = 1.68 * 10^{-5} \cdot G^{0.7625} \cdot x^{0.22} \,, \tag{19}$$

for $\dot{r}$ in m/s, G in kg/m^{2}s and x in m. Using these Marxman parameters, the average relative error between the experimental final diameter and the numerical one amounts to 6.2 %. Interestingly, the exponent $b = 0.22$ for the axial distance changed its sign to a positive value as compared to the negative sign in Eq. 18. We will discuss the regressing behavior of the multi stepped grains in the coming section in detail, at this point as a first observation we notice that with increasing axial distance, the effect of the steps on the regression seems to be augmenting (visible in the positive value for b). This is visible in the bigger distance between the initial and final diameter in Figure 4, but also in the decreasing distance between the FFS and BFS in the final diameter profile (red line).

5.3. Definition of Optimization Criteria and Polynomial Degree

To derive the (semi-) optimal profiles, we have to decide on the importance of each optimization criteria for the algorithm according to Equation 14. It is necessary to understand how different weighing of the criteria changes the optimized initial fuel port profiles. Three cases are to be differentiated:

1. **Max. weight at Q_1:** Means that minimal variation of O/F throughout the burn is the most important criteria. The algorithm creates an initial profile that has a large initial diameter. This is because the initial mass flux for high diameters is lower, and therefore the regression rate is also lower. With a low regression rate, the fuel port changes slower than compared to high mass fluxes and, thus, the variation of the O/F over time is smaller.

2. **Max. weight at Q_2:** The algorithm favors an average O/F which is closest to stoichiometry (in the case of HDPE/H_2O_2 it is around 7). This leads to two scenarios. a) the algorithm favors a low regressing solution that leads to a low shifting O/F grain with a value close to stoichiometry. Dependent on the Marxman empirical parameters, this solution could not exist. b) The algorithm favors a higher shifting O/F solution, however, the average remains close to stoichiometry. For example, a solution where the O/F starts at 4 and ends at 10, yields an average O/F of 7.
3. **Max. weight at Q_3:** This leads to the algorithm converging to an initial profile which is very close to the maximal allowable fuel port diameter (the motor casing diameter). Simply put: a hypothetical fuel grain with this diameter would be consumed in total within a short time. With this, no residuals remain. From the point of view of the algorithm, which only judges quality based on the residuals, these profiles are optimal.

Concluding this different behavior of the algorithm based on the weighting, we decided on a distribution of:

$$\begin{aligned} \text{minimal variation } (Q_1) &: w_1 = 5 \\ \text{optimal O/F } (Q_2) &: w_2 = 10 \\ \text{minimal residues } (Q_3) &: w_3 = 1 \end{aligned}$$

Based on testing different weight combinations, the results with this combination were leading to the most reasonable initial fuel port profiles. It is to be said that even for a constant weighing of quality criteria, the shape and type of the optimal profiles for each run can vary greatly, as it has been shown in previous work.[19] This is due to the fact that the genetic algorithm cannot find a true optimum, but rather finds multiple semi-optimized profiles.

5.4. Optimized Profile

Before we can obtain the initial fuel port geometry, we need to decide on the polynomial degree for the approximation. We opted for a polynomial degree of third order, hoping to obtain fuel port geometries that allow more possibilities to distribute steps along the profile. Nonetheless, we are aware that this choice is rather arbitrarily. The other parameters used for the algorithm are presented in Table 1.

Figure 5 shows the (semi-) optimal profile for a multi-stepped profile in the HYCAT engine. In the same image, we also plotted the two types of cylindrical fuel port diameters (25 mm and 40 mm) that are usually employed in a HYCAT test. The first observation is that the profile oscillates around a hypothetical constant mean value. Interestingly, this value is close to the 40 mm fuel port. Therefore, it will be interesting to compare the results of both cases in the later sections. The shape of the optimal profile can further be explained recalling Figure 4: with the a, b, n values obtained from the alternating step case the regression rate of the grain is higher downstream the motor than near the head end. On the other hand, in any HRE, the regression rate is strongly related to the mass flux and hence the fuel port diameter (with increasing port diameter the regression rate decreases). With this information, the shape of the optimized profile can be understood. The regression rate of the alternating profile is lowest at the beginning of the grain and increases constantly until the end of the grain. In the optimized profile, the smaller port diameters are upstream, while the larger port diameters are downstream. Given the inverse proportionality of regression rate to fuel port diameter ($\dot{r} \propto 1/D^2$), theoretically, the fuel port change over the total fuel grain length (and as a consequence the O/F shift) should be more constant. Moreover, the optimized profile oscillates around a rather large initial fuel port diameter. Usually, such a high initial fuel port diameter leads to higher O/F values for cylindrical grains in our engine, however, since the multiple steps increase the average regression rate considerably, lower O/F values can be achieved at these larger fuel port diameters.

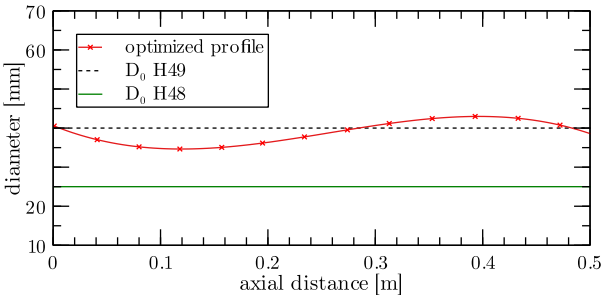

Fig. 5. Optimized profile compared to reference fuel port diameters.

5.5. Approximating the Profile with Steps

Here, we approximate the optimized profile shown in Fig. 5 with steps. Theoretically, such profiles could be 3D-printed, however this limits fuel choice, density control and large scale applications (for the current state of the art). Moreover, a stepped profile can increase regression rates through the stepped geometry. Hence, in this section, we approximate the optimized profile with steps (which represent fuel grain segments with different inner diameters).

Based on our previous work on single steps (Refs. 1, 2) the approximation approach is the following:

1. Add a tolerance to the profile generated with the algorithm. To test the behavior of the approximation, two tolerance levels are applied: i) 10 % and ii) 20 %.
2. For both cases, keep at least the first 50 mm axial distance untouched to profit from the injector effects (increased regression due to recirculation zone).
3. Distribute steps according to the rule of thumb developed in previous work:[1,2] BFS profit from long undisturbed flows after the step and should therefore be spaced with larger distances between the steps. As for the step height, the higher, the better (until 10 mm tested so far numerically[1]). For FFS, the zone of influence is shorter, and the steps should be distributed more frequently.
4. Two types of approximations are followed: i) a fine approximation of the profile with step heights 2 mm (FFS) and 4 mm (BFS). ii) The profile is approximated with larger steps that are spaced more coarsely. In fact, the number of steps is fixed to six, close to the number of steps as the alternating profile of H55. The step heights are 4 mm for FFS and 8 mm for BFS.

Figure 6 displays both profiles and the stepped approximation. For a more convenient interpretation of the curves, the diameters are the motor diameter (rounded to 100 mm) minus the inner diameter. This way, the steps are illustrated the same way as they would be on a flat plane with steps.

Table 1. Parameters for algorithm.

Max. iterations	Polynomial degree	Individuals	w_1	w_2	w_3	a	n	b
10000	3	15	5	10	1	$1.68*10^{-5}$	0.7625	0.22

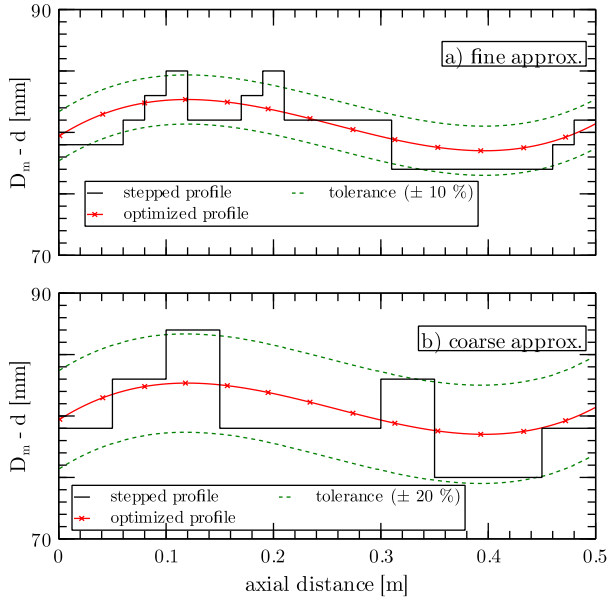

Fig. 6. Approximated optimized profile. a) fine approximation, b) coarse approximation.

In Figure 6, the best practices to distribute steps become more visual. FFS are followed by a next step considerably earlier than BFS.

6. Experimental Results

All experimental data are obtained from the HYCAT facilities (see Section **3.1.**). Table 2 lists the experimental results of the tests. Additionally, tests H48 and H49 are documented, which are cylindrical cases without steps. Moreover, for comparison, we added tests with single FFS (H50) and single BFS (H52) from a previous study.[1,2)]

The average mass flux is calculated using the average fuel port diameter throughout the burn, following the recommendation of Ref. 21):

$$G_{\mathrm{ox,avg}} = \frac{4\,\dot{m}_{\mathrm{ox}}}{\pi\, D_{\mathrm{avg}}^2}\,, \tag{20}$$

with the average port diameter during the burn denoting to:

$$D_{\mathrm{avg}} = \frac{\overline{D}_0 + D_f}{2}. \tag{21}$$

$\overline{D}_0$ is the average initial diameter. Since the multi-stepped fuel grains consist of different slices with different inner diameter and length, the average fuel grain diameter in these cases needs to be calculated using a weighted average:

$$\overline{D}_0 = \frac{\sum_1^S D_{0,i} * L_i}{\sum_1^S L_i}\,, \tag{22}$$

where $D_{0,i}$ is the fuel port diameter of the i-th slice and L_i the length of the i-th slice and S the total number of slices. The average regression rate ($\dot{r}$) is estimated using the mass loss method (Section **3.2.**). The results of the tests are discussed in detail in the following subsections.

6.1. Alternating Profile of H55

Figure 7 displays the experimental results of the alternating step profile (H55) in detail. The following elements are displayed in the illustration:

1. Local regression rate (Figure 7a)
2. Initial versus final diameter (Figure 7b). Note that the diameter displayed is the outer motor diameter (D_m) minus the inner diameter. This way the profile can be interpreted as the lower half of the scan in Figure 7c)
3. Indication to distinguish between BFS and FFS for Figure 7a) and b).
4. 2D Scan of fuel port geometry after the test (Figure 7c)

a) regression rate profile

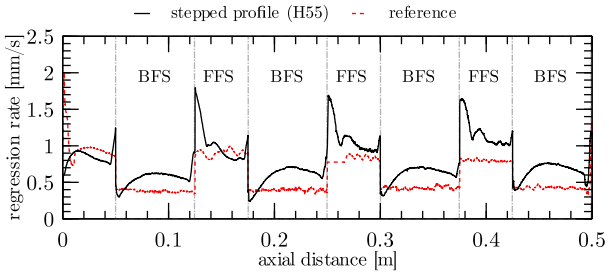

b) initial vs. final diameter

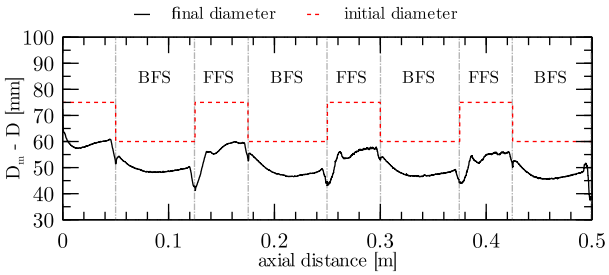

c) scanned image after cut

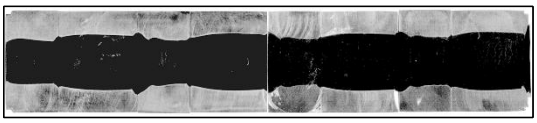

Fig. 7. H55 profiles (alternating steps).

Since the alternating stepped profile consists of fuel grain segments of 25 mm and 40 mm, it is possible to compare them to the tests H48 (D_0=25 mm) and H49 (D_0=40 mm) with no steps.

Looking at the regression rate profiles of H55 in Figure 7a), the different effect of the BFS and FFS can be easily observed. For BFS, directly after the step, the regression rate drops below the reference case but increases shortly further downstream significantly over the reference regression rate. This is because

Table 2. Summary of experimental data.

Test	$\overline{D}_0$ [mm]	t_b [s]	$\dot{m}_{ox}$ [kg/s]	O/F [-]	$G_{ox,avg}$ [kg/m^{2}s]	$\dot{r}$ [mm/s]	Δm_f [g]	P_c [bar]	η [%]
H48 (Ref.)	25.0	9.65	0.337	7.96	388.02	0.86	408.9	26.1	87.0
H49 (Ref.)	40.0	9.65	0.348	12.58	228.02	0.42	266.7	24.1	88.8
H50 (FFS)	32.5	9.60	0.343	10.19	299.37	0.59	322.8	25.4	89.1
H52 (BFS)	32.5	9.66	0.346	8.84	289.59	0.67	378.2	28.3	95.4
H55 (alternating)	34.0	9.44	0.326	6.66	241.52	0.79	462.2	27.9	94.3
H56 (fine)	40.1	9.51	0.337	9.59	211.46	0.52	334.2	25.9	90.6
H57 (coarse)	40.4	9.60	0.344	8.83	208.36	0.57	374.4	26.8	89.6

directly after the step, the flame is further away from the fuel surface and, thus, the surface temperature is lower. With the surface temperature being a detrimental driver for the regression rate,[1,2)] the regression rate directly behind the BFS decreases. At the reattachment point of the flow, however, the regression rate increases and because of the augmented mixing and turbulence induced by the recirculation zone behind the step, the regression rate increases over the reference at a constantly higher level. For the FFS, the behavior is different: the FFS pushes the flame away from the surface already before the step, thus, decreasing the regression rate. After the FFS, two peaks in regression rate are visible. The first peak is due to the lateral progression of the FFS. Given the way the regression rate is calculated (final diameter minus initial diameter divided by the burn time), lateral fuel consumption (instead of radial regression) leads to these discontinuities. However, the second peak is the point of the reattachment of the flow and the increased mixing and turbulence shows itself in higher regression rates. Notably, the peak of the regression rate for FFS is considerably shorter than in the case of BFS, because for an FFS the diameter after the step is smaller and the flow accelerates.

We showed the aforementioned different effects of FFS and BFS on single stepped grains already numerically[1)] and experimentally.[2)] However, in this work, we can investigate the interdependence of multiple steps for the first time. Three major observations are to be noted:

1. The shape of the regression rate profiles for BFS or FFS is very consistent throughout the profile, and it is unique to the type of step.
2. When an FFS follows a BFS, the regression rate drops already further upstream than for a single FFS.
3. The difference between the reference cases and the H55 profile increases further downstream. For the first 3 BFS, the H55 regression rate decreases for a short distance below the reference. At the last BFS, the regression rate still decreases directly after the step, however, it is constantly above the reference. The same is true for the FFS. While the regression rate of the first FFS drops below the reference cases, the other two FFS profiles are constantly above the reference. This proves that the regression rate increasing effects of steps can accumulate to considerably augment the average regression rate, rather than interfering negatively between each other.

In Section **6.4.**, we will quantify the accumulation of average regression rates through multiple steps by consulting the time- and space averaged regression rates of all multi-step profiles.

6.2. Fine Optimized Profile of H56

In this section, we assess the optimized profile, which is closely approximated with small steps (2 mm for FFS and 4 mm for BFS). Similar to the alternating profile of the previous section, in Figure 8, the fuel grain scan after the test, the initial and final diameter as well as the regression rate profile is displayed.

a) regression rate profile

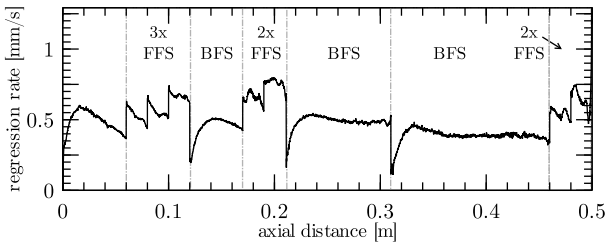

b) initial vs. final diameter

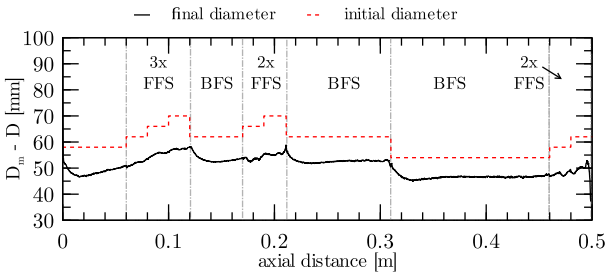

c) scanned image after cut

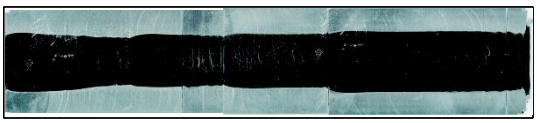

Fig. 8. H56 profiles (optimized profile, fine approximation).

The most prominent observation is that the profile that is visible in the scan of Figure 8c) is almost completely smooth and the steps vanished. Only the markings left by the recirculation zones show the traces of the steps. This observation leads to the conclusion that the step heights of 2–4 mm are disappearing after at least 10 s burn time for our set-up. Consequently, with increasing burn time, the steps progress and the fuel port becomes smooth, and we achieved to obtain a smooth profile that we wanted to approximate with steps.

Since this profile is approximated with 10 steps, we can investigate how multiple steps interact with each other. Looking at the regression rate profiles in Figure 8a), it is surprising how

consistent the characteristic shapes of the BFS and FFS regression rate profiles are: for the FFS, the first peak (discontinuity to be more precise), which displays the lateral progression of the step, is visible, followed by are smaller peak that shows the increase in regression rate due to the recirculation zone. Especially looking at the first triple of FFS, the resemblance of the shape is surprising.

For the BFS, likewise, the shape of the regression rate is similar across all BFS. The decrease in regression rate directly after the step because of the flame being further away from the surface is followed by a considerable increase in regression. Additionally, it is visible that when an FFS follows on a BFS, the regression rate at the end of the BFS zone decreases because of the flame being pushed further away from the surface. For example, consider the shape of the regression rate profile of the first BFS and the second BFS. At the first BFS, the profile has a strongly concave shape (thus the regression rate decreases before the next FFS). For the second BFS, however, the regression rate profile is almost constant. The same effect was already visible in the alternating profile.

Looking at the initial vs. final diameter in Figure 8b), it becomes clear that the steps completely disappeared within 10 seconds. It is therefore of interest, how the coarse profile with larger steps of H57 performs in the next section.

6.3. Inverted Coarse Profile

We present the test of the profile approximated with fewer but taller steps now. The total number of steps is 6 (close to the alternating profile H55) and the height varies between 4 mm and 8 mm. Unfortunately, during the assembly and preparation of the motor, we inserted the fuel grain the wrong way around, meaning that the profile was inverted. Figure 9 shows the planned profile and compares it to the profile that was tested in reality because of the wrong preparation of the motor. While this accident eradicated the primary goal in testing optimized profiles (a new test is scheduled for an extension), it still gives us valuable data whether our defined rule of thumb is valid or not. To recall, based on previous research on single steps, we

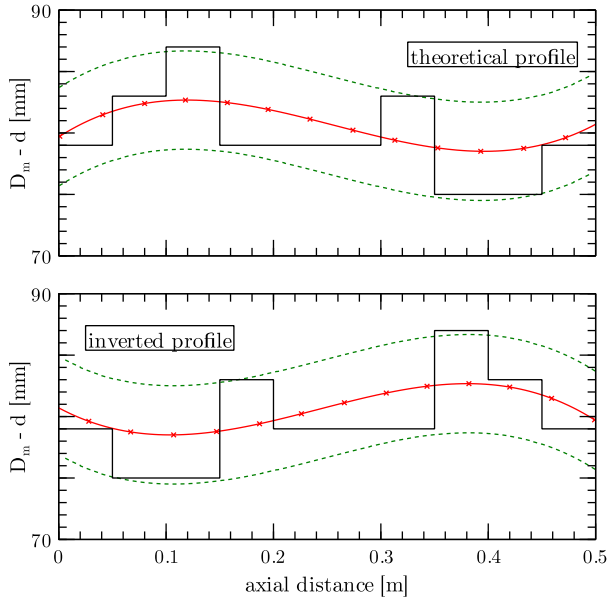

Fig. 9. Inverted profile of H57.

postulated that BFS should be as tall as possible and spaced further from a next step. For FFS, the height should be limited, and they are preferably spaced close to a next step. By accidentally inverting the profile on H57, we can now test this hypothesis because the inverted profile is now exactly opposite to what was desired: many small BFS (4 mm) followed by a few tall FFS (8 mm).

Figure 10 displays the experimental data (scan, diameter, regression rate) of the inverted profile. Looking at the regression rate profile of H57, it can be noted that overall, the shapes unique to the type of step are still valid for all steps. Interestingly, for the FFS, the second peak of regression rate increase is almost measurable for the whole length of the FFS. This leads to the conclusion that the length-to-height ratio (x/h) of this profile is close to the optimum spacing. For H55 (alternating profile) the x/h was around 7, in the present coarse profile it decreased now to 6, which seems to be almost the optimum. For the BFS cases, however, it is visible that the regression rate profiles for the first two BFS are not constant but are decreasing. We predicted this effect numerically[1)] already: BFS need a certain height (numerically it was above 5 mm) to show a constant increase in regression rate for the remainder of the grain. Below this threshold, the regression rate profile resembles more an FFS, where a peak is visible that decreases with increasing distance. In Figure 10a), we can observe that the BFS regression profiles have a distant peak and then decrease with axial distance. Meaning that the step height for BFS (4 mm) for the inverted profile of H57 is too low to constantly increase the regression rate, as it was for the BFS in H55 (7.5 mm step height). Another interesting observation is the difference of transition from BFS to FFS. In H55 (Fig. 7), between BFS and FFS a clear cavity was visible, showing lateral regression of the grain both upstream and downstream. In H57 (Fig. 10), the transition is smooth without clear cavity. We suspect the cause for this discrepancy in the height of the BFS before the FFS: in H55, the BFS is 7.5 mm and (considering the discussion above) more powerful to increase the regression rate through the recirculation zone and turbulence. When this more turbulent flow impinges on the FFS, the recirculation zone before the FFS creates the cavity for H55. In H57, because of the smaller, less powerful BFS before the FFS, this effect is slightly visible, but considerably less pronounced.

Keeping in mind also, that the cavities occur where the different grain segments are assembled (but only for the transition from BFS to FFS). This could promote the formation of a cavity too.

6.4. Time- and Space Averaged Regression Rates

In previous sections, we assessed the effect of multiple steps on the local regression profiles. In this section, we investigate the time- and space averaged regression rates to obtain information on the complete fuel grain throughout the burn. In Figure 11, the temporal and spatial averaged regression rate is plotted.

The average regression rate $\dot{r}$ is estimated using the mass loss method (Section **3.2.**). Using the points of the reference cases (H46-H49), the best fit for the Marxman law (without local dependency x) is plotted. Moreover, the tests with single steps of BFS (H52) and FFS (H50) are indicated from previous work.[1,2)] The relative augmentation of regression rate for all cases to the reference curve are given in percent next to the data points.

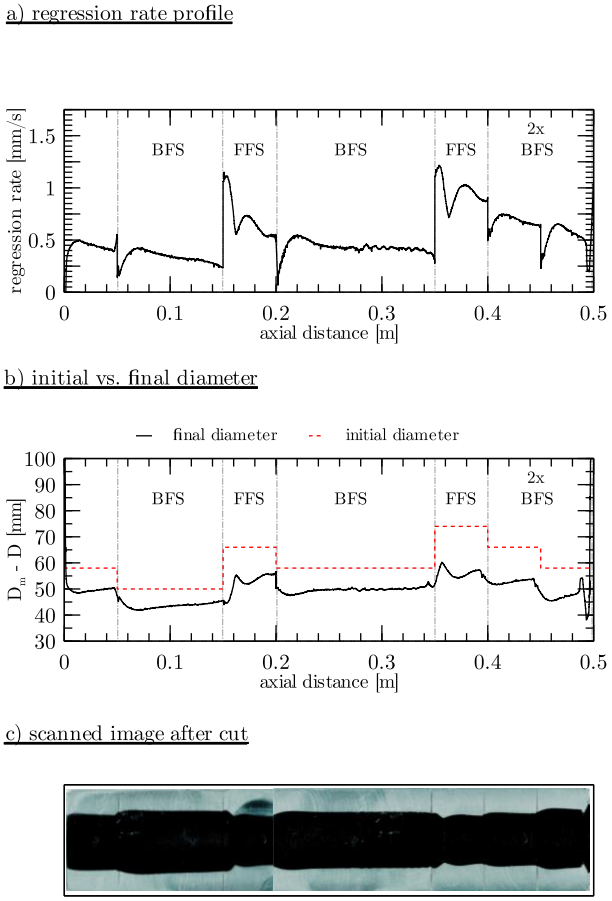

Fig. 10. H57 profiles (inverted optimized profile, coarse approximation).

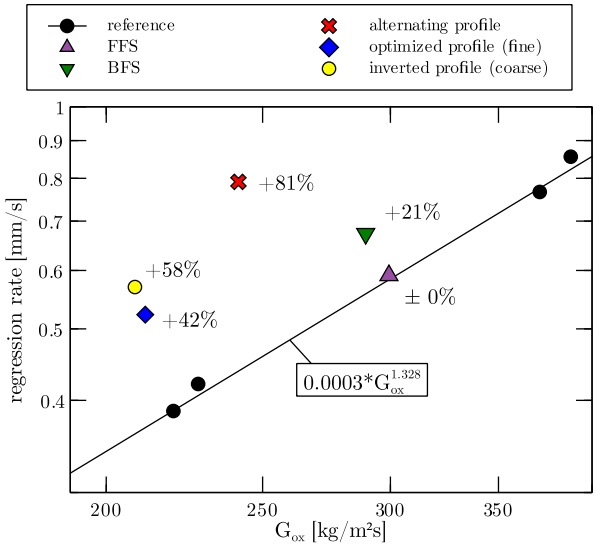

Fig. 11. Time- and space averaged regression rates.

Looking at Figure 11, it is visible that a single FFS (H50) cannot increase the regression rate noticeably over the total fuel grain, because the zone of higher regression rates is too short to have an impact on the total fuel grain length. On the other hand, a single BFS (H52) increases the regression rate by 21 % because the regression rate after the step is increased at a constant level over the remainder of the fuel grain.[2)] Based on these observations, the alternating fuel grain (H55) was created with 7 steps in total (4 BFS and 3 FFS). The total regression rate increase amounts to 81 % on average for the total burn duration. Recalling the regression rate profiles of the alternating profile in Section **6.1.**, it became obvious that the effect of steps can be accumulated by deploying multiple steps (similar to what has been reported by Sakashi *et al.*[11)] and Kumar and Joshi[12)]). With H55, we also created a multi-stepped baseline, which allows us to assess the effect of the optimization on the average regression rate for test H56 (fine profile) and H57 (inverted coarse profile).

Looking at H56, the regression rate increase dropped to 42 % although more steps (10 in total, 7 FFS and 3 BFS) are used. The reason for this behavior is two-fold: first, more FFS than BFS are used. Based on our lessons learned, FFS are less performing than BFS, considering only the regression rate augmentation. Therefore, a slight drop in total regression rate increase was to be expected. Moreover, in order to have a fine approximation of the optimized profile (recall Fig. 6), the step height was significantly reduced to 2 mm for FFS and 4 mm for BFS. Compared to the 7.5 mm of H55, it seems that the height of the step has a driving effect on the total regression rate increase. Finally, considering the final profile of the cut fuel grain in Figure 8 for H56, we observed that the steps vanished during our burn time due to their smaller sizes. This signifies that most probably the effects of the steps were also vanishing over time, thus, leading to a lower total regression rate augmentation.

Turning our attention to H57 (inverted coarse profile), it is to be reminded that during the preparations of the tests we accidentally mounted the fuel grain in a wrong orientation leading to an inverted profile, which is exactly contradictory to what we wanted to achieve. The grain has now few but tall FFS and small but many BFS. Nonetheless, this allows us to test our postulation. The inverted profile consists of 4 BFS (4 mm height) and 2 FFS with 8 mm height.

The total regression rate increase for H57 re-gained some percentages, up to 58 %. The main reason for this increase is that the height of the steps in H57 was increased to 4 mm for FFS and 8 mm for BFS. Interestingly, although the profile is inverted (thus not following our rule of thumb for distribution of the steps), the regression rate of H57 is considerably higher than that of H56 where we followed the distribution rule. This leads to the important conclusion that the positioning of the steps based on the type (FFS vs. BFS) is less important than the relative height of the steps, if the steps are too small to sustain the total burn time. However, compared to the alternating profile of H55 where the tall steps (7.5 mm) are spaced according to our heuristic distribution rule, the regression rate of H57 (58 %) is still below the 81 % of H55. This underlines that the distribution of steps (while being less important than the total step height) still plays an important role. We expect to obtain regression rate values closer to H55 when re-doing H57 with the proper grain orientation.

Summarizing, the optimized profiles of H56 and H57 lost some of the total regression rate increase when compared to the simple alternating grain of H55 (but still considerably above the reference cases). However, the profiles of H56 and H57 were not only created to increase the regression rate, but also optimized to obtain O/F values closer to stoichiometry and a lower O/F shift during the burn. In the next section, we will discuss

whether the optimized profiles (created for constant O/F and O/F ratios closer to stoichiometry) justify the loss in regression rate augmentation.

6.5. Results of Ballistic Reconstruction

In this section, we discuss the temporal evolution of the oxidizer to fuel ratio (O/F) and the regression rate according to the ballistic reconstruction method explained in Section **3.4.**. The reconstructed values are compared for the tests H48-50, H52 and H55-H57. The reference cases H48 and H49 are included to judge the change in ballistic behavior from no-step cases to multi-stepped profiles. The results are plotted in Figure 12. Additionally, to the temporal evolution obtained from the reconstruction, the average regression rates and O/F ratios obtained from the mass-loss method are plotted. Since these values are independent of the O/F reconstruction, it allows us to judge whether the reconstructed values are following a logical trend.

Looking at the regression rate of the reference cases H48 and H49, it appears almost constant throughout the burn. Considering that H48 (experimental *final* diameter 42 mm) and H49 (*initial* diameter 40 mm) could be interpreted as one long continuous burn, this result of the ballistic reconstruction is surprising. Between H48 and H49, the regression rate drops from values around 0.8 mm (H48 end of burn) to 0.5 mm (H49 beginning of burn). In reality, a more consistent decrease in regression rate should be expected. It seems that the assumptions made in Section **3.4.** could lead to this differing behavior.

Nonetheless, with these two tests, we can establish a reference behavior of regression rate and O/F to compare to the stepped cases. As for the O/F in Figure 12a), the trend is slightly decreasing for H48 and H49 (less pronounced). This is due to the regression rate being almost constant, while the port diameter increases over time. Hence, the burning surface increases over time, while the regression rate remains constant, leading to a decreasing O/F over time. In H49, the average regression rate is considerably smaller due to the lower average mass flux. That is why the decreasing O/F effect for H49 is less pronounced.

Starting with the single stepped cases of H50 (FFS) and H52 (BFS) (Figure 12b)) the regression rate drops over time. This is because of the step vanishing over time and, thus, the regression rate increasing effects slowly decreasing too. Interestingly, the O/F for H50 and H52 is staying almost constant. This signifies that the regression rate of the single stepped cases decreases in the same order of magnitude as the burning surface increases over time. As a consequence, the O/F remains constant.

The effect of diminishing steps becomes strongly visible for the multi-stepped cases H55-57 in Figure 12c). At the beginning of the burns, the regression rate stays rather constant, but with increasing burn-time, the regression rate drops significantly. This behavior is more pronounced for the cases with higher steps (H55 & H57) than for the smaller stepped case H56. For all multi-step cases, initially, the O/F remains constant (in fact, all initial O/F values are close to the optimized stoichiometry of 7). As soon as the regression rate drops (because of the steps diminishing over time) the O/F increases sharply. This is because the high initial regression rates of the multi-step grains increase the fuel port diameter fast, thus, reaching low mass flux levels rather quickly. Once the steps have progressed, the regression rate effect (and the fuel mass flow) decreases significantly and therefore the O/F increases considerably. In fact, the O/F of the multi-stepped cases catches up to the average O/F of H49 (reference case with 40 mm initial fuel port diameter) because the diameters of the multi stepped grains are approximately in the same order of magnitude. In other words, the multi-stepped grains increased the regression rates initially to such an extent that the O/F values of the grains (although being at low mass fluxes) were in a reasonable range. After the steps vanished, the regression rates and, thus, the O/F values approach the ballistic behavior of the low mass flux reference case H49.

It is to be stressed, again, that the assumptions made when presenting the ballistic reconstruction are likely to have a bigger impact on results of the reconstruction method. Three major limitations are to be pointed out:

1. Due to the steps, the inner surface (S) of the grains increases as compared to a grain with the same representative diameter but without steps. For H55 the burning surface increases by 10 % because of the steps, for H56 by 4.8 % (due to the smaller steps) and for H57 the initial surface is 8.3 % larger. This cannot be considered in our current reconstruction method. Since the total fuel mass flow is dependent on the burning surface, the ballistically reconstructed regression rate tends to be higher than the true one (lower burning surface at the same fuel mass flow means higher regression rate) according to:
$$\dot{m}_{\text{fuel}} = \rho_f \, \dot{r} \, S \ . \tag{23}$$
Moreover, as the steps regress, the difference in initial burning surface between stepped and no-stepped grains becomes less pronounced. This renders the estimation of the proper regression rate throughout the total burn time difficult.
2. We impose a constant combustion efficiency (in fact, the reconstruction method iterates over different constant efficiencies until the total reconstructed mass loss matches the experimental one). However, during each iteration, the efficiency stays constant. This assumption is already considered delicate for cylindrical grains,[16] however, for stepped grains this assumption poses an even bigger deviation: with larger steps (beginning of burn) the mixing and, hence, the combustion efficiency is higher than at the end of the burn where the steps already regressed.
3. The throat diameter is considered constant. This assumption in reality is not true because the ablatively cooled graphite nozzles erode over time, thus constantly enlarging the throat diameter. Indeed, in H57, shortly before 4 s burn time, we observed increased erosion, visible in a drop in chamber pressure and rise in oxidizer mass flow.

Nonetheless, the ballistic reconstruction method – with all its limitations – allows to qualitatively investigate the temporal O/F ratios and regression rates. As a proof of quality, the experimentally obtained temporal and spatially averaged regression rates from the mass loss method (which is completely independent of the ballistic reconstruction) are plotted alongside the values calculated with the reconstruction method. We can see that the average values match the reconstructed values sufficiently well.

While this section was able to give insights into the qualitative temporal behavior of the O/F, due to the aforementioned

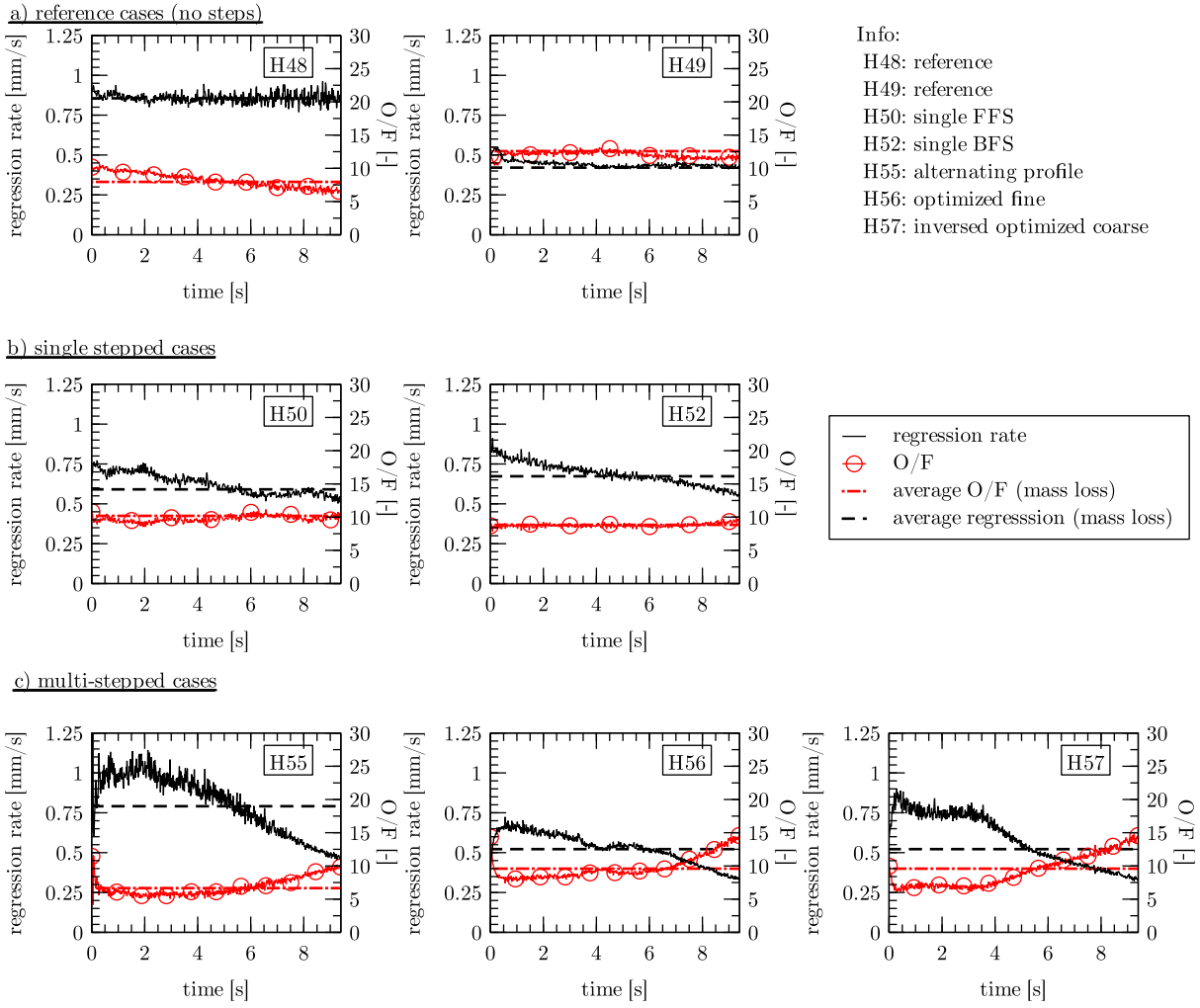

Fig. 12. Results of ballistic reconstruction.

drawbacks of the O/F reconstruction with stepped geometries, it is impossible to conclusively judge whether our optimized profiles decreased the O/F shift or not. Indeed, in the beginning of the burn of H55-H57 the O/F value remains constant, however, towards the end of the burn the O/F value increases considerably. For the reference cases H48 (with limitations) and H49, the O/F is constant throughout the burn. It is therefore questionable whether the optimized profiles minimized the O/F shift or not. Nonetheless, in all cases, the total regression rate was increased considerably.

7. Conclusion

In this work, we investigated the impact of optimized multi-stepped profiles on the regression rate and the oxidizer-to-fuel ratios. In order to obtain the optimized profiles, we created a genetic algorithm that allows to optimize fuel grain profiles according to optimization criteria like low oxidizer-to-fuel shift and mixtures closer to stoichiometry. However, we like to stress that a multitude of different optimization criteria can be implemented into the genetic algorithm. Additionally, the genetic algorithm allows obtaining empirical Marxman parameters (even for the spatial resolution x) using only a single test instead of a combination of reference tests.

A total of three different fuel grain profiles were created: a) an alternating profile with 3 forward facing steps and 3 backward facing steps of 7.5 mm height, b) an optimized profile where the fuel port is approximated closely by 10 steps of 2–4 mm height, c) the same optimized profile that is approximated coarsely by 6 steps (4–8 mm).

The tests of the grains a)–c) were conducted on the HYCAT engine and the local regression rate profiles as well as the time- and space averaged regression rates assessed. The following observations are to be noted:

1. The characteristic shape of the regression rate profile for each step type (forward vs. backward) was almost identical for all tests, proving that the mechanisms behind the regression rate increase are the same for different step heights (from 2 mm to 8 mm), step distributions and mass-flux levels.
2. In the case of step heights between 2 mm and 4 mm, for our 10 s tests, the steps vanish and leave a smooth profile which is close to the initial profile that needed to be approximated.
3. The step height has a more pronounced effect on the regression rate increase than the proper distribution of the steps. In other words, if only the regression rate needs to

be increased to a maximum, it is more important to employ higher steps rather than distributing them according to their area of influence.
4. The optimization of profiles and its approximation with steps dictates the distribution of the steps. In our cases, this leads to lower regression rate increases than a purely alternating profile (42–58 % vs. 81 %)
5. It is expected that when grains with similar step heights are compared, the proper distribution (long backward facing steps and short forward facing steps) becomes important again.
6. The optimized profiles showed mixture ratios close to the value they were optimized for. However, it could not be conclusively assessed whether it is the optimization that improved the mixture ratio. The optimized profile has a higher average initial diameter than the alternating reference profile, therefore changing the mixture ratio already without changing the fuel port profile shape – simply by having a higher average initial diameter. It is possible that an alternating step profile (no optimized profile) at the same average initial diameter has the same effect on the mixture ratio than the optimized profile.
7. Short burn times (up to 10 s) and/or motor designs that show already rather horizontal regression without optimization limit the possibilities for the genetic optimization algorithm. We postulate that with larger burn times and – more importantly – larger fuel grains, the optimization of the mixture ratio shift becomes significantly more important.

To conclude, we have shown that multiple steps can increase the regression rate of hybrid engines considerably (up to 81 %; we suspect the limit is not yet reached). Moreover, the genetic algorithm developed proved a powerful tool to obtain the Marxman empirical values with a single test.

Regarding the optimization for the mixture ratio, the results were inconclusive because of short burn times and a motor design that burns already rather horizontal even without optimization. Nonetheless, we would like to stress that the way to obtain our (semi-) optimized combustion chamber designs is by no means limited to the genetic algorithm. We have laid the foundation of a method to approximate numerous combustion chamber designs by a set of different fuel grain cylinders that are assembled; allowing to tailor the performance of hybrid rockets to a wide range of use-cases.

Acknowledgments

The authors would like to thank the technical experts of ONERA for the support of the test campaigns.

Funding: The project leading to this application has received funding from the European Union's Horizon 2020 research and innovation programme under the Marie Sklodowska-Curie grant agreement No 860956. It is part of the ASCenSIon project, an Innovative Training Network (ITN) to advance space access capabilities (https://ascension-itn.eu/).

References

1) C. Glaser, J. Hijlkema, J. Y. Lestrade, and J. Anthoine. Influences of steps in hybrid rocket engines: Simulation and validation on simplified geometries. *Acta Astronautica*, March 2023.
2) C. Glaser, R. Gelain, A. E. M. Bertoldi, Q. Levard, J. Hijlkema, J. Y. Lestrade, P. Hendrick, and J. Anthoine. Experimental regression rate profiles of stepped fuel grains in Hybrid Rocket Engines. *Acta Astronautica*, 204:186–198, March 2023.
3) C. Glaser, J. Hijlkema, J. Y. Lestrade, and J. Anthoine. The stepped helix hybrid rocket engine. In *AIAA Aviation Forum, San Diego*, 2023.
4) G. Marxman and M. Gilbert. Turbulent boundary layer combustion in the hybrid rocket. *Symposium (International) on Combustion*, 9(1):371–383, January 1963.
5) Dario Pastrone. Approaches to low fuel regression rate in hybrid rocket engines. *International Journal of Aerospace Engineering*, 2012, 2012.
6) Christopher Glaser, Jouke Hijlkema, and Jerome Anthoine. Evaluation of Regression Rate Enhancing Concepts and Techniques for Hybrid Rocket Engines. *Aerotecnica Missili & Spazio*, May 2022.
7) P. A. O. G. Korting, H. F. R. Schöyer, and Y. M. Timnat. Advanced hybrid rocket motor experiments. *Acta Astronautica*, 15(2):97–104, February 1987.
8) Landon Kamps, Kazuhito Sakurai, Yuji Saito, and Harunori Nagata. Comprehensive data reduction for N2O/HDPE hybrid rocket motor performance evaluation. *Aerospace*, 6(4), 2019.
9) Jungpyo Lee, Sunjae Rhee, Jinkon Kim, and Heejang Moon. Combustion Instability Mechanism in Hybrid Rocket Motors with Diaphragm. *Journal of Propulsion and Power*, pages 1–10, October 2021.
10) Omer Musa, Guoping Huang, and Zonghan Yu. Effects of new solid propellant configurations on the combustion characteristics of a ramjet. *Aerospace Science and Technology*, 119:107192, December 2021.
11) Hatagaki Sakashi, Yuasa Saburo, Hirata Kousuke, and Sakurai Takashi. Effectiveness of Concave-convex Surface Grain for Hybrid Rocket Combustion. *48th AIAA/ASME/SAE/ASEE Joint Propulsion Conference and Exhibit*, July 2012.
12) Manish Kumar and P.C Joshi. Regression rate study of cylindrical stepped fuel grain of hybrid rocket. *Materials Today: Proceedings*, 4(8):8208–8218, 2017.
13) Jean-Yves Lestrade, Jérôme Anthoine, Onno Verberne, Adrien J. Boiron, Gaël Khimeche, and Christophe Figus. Experimental demonstration of the vacuum specific impulse of a hybrid rocket engine. *Journal of Spacecraft and Rockets*, 54(1):101–108, jan 2017.
14) Arif Karabeyoglu, Greg Zilliac, Brian J. Cantwell, Shane DeZilwa, and Paul Castellucci. Scale-Up Tests of High Regression Rate Paraffin-Based Hybrid Rocket Fuels. *Journal of Propulsion and Power*, 20(6):1037–1045, November 2004.
15) Johannes Schindelin, Ignacio Arganda-Carreras, Erwin Frise, Verena Kaynig, Mark Longair, Tobias Pietzsch, Stephan Preibisch, Curtis Rueden, Stephan Saalfeld, Benjamin Schmid, Jean-Yves Tinevez, Daniel James White, Volker Hartenstein, Kevin Eliceiri, Pavel Tomancak, and Albert Cardona. Fiji: an open-source platform for biological-image analysis. *Nature Methods*, 9(7):676–682, July 2012.
16) Jerome Messineo, Koki Kitagawa, Carmine Carmicino, Toru Shimada, and Christian Paravan. Reconstructed Ballistic Data Versus Wax Regression-Rate Intrusive Measurement in a Hybrid Rocket. *Journal of Spacecraft and Rockets*, 57(6):1295–1308, November 2020.
17) Elena Quero Granado, Giulio Pelenghi, Jouke Hijlkema, Jean-Yves Lestrade, and Jerome Anthoine. A new System Design Tool for a Hybrid Rocket Engine Application. In *73rd International Astronautical Congress*, September 2022.
18) S. Gordon, B.J. McBride, United States. National Aeronautics, Space Administration. Scientific, Technical Information Branch, and Lewis Research Center. *Computer Program for Calculation of Complex Chemical Equilibrium Compositions, Rocket Performance, Incident and Reflected Shocks, and Chapman-Jouguet Detonations*. NASA SP. Scientific and Technical Information Office, National Aeronautics and Space Administration, 1976.
19) Jouke Hijlkema. A presentation of a complete design cycle for optimised hybrid rocket motors. In *SpacePropulsion 2018, Seville*, 2018.
20) C. Carmicino and A. Russo Sorge. Influence of a conical axial injec-

tor on hybrid rocket performance. *Journal of Propulsion and Power*, 22(5):984–995, sep 2006.

21) M. Arif Karabeyoglu, Brian J. Cantwell, and Greg Zilliac. Development of Scalable Space-Time Averaged Regression Rate Expressions for Hybrid Rockets. *Journal of Propulsion and Power*, 23(4):737–747, July 2007.